HHS Public Access

Author manuscript

Cell Rep. Author manuscript; available in PMC 2019 August 26.

Published in final edited form as:

Cell Rep. 2019 August 06; 28(6): 1499–1510.e6. doi:10.1016/j.celrep.2019.07.007.

Expansion of Luminal Progenitor Cells in the Aging Mouse and Human Prostate

Preston D. Crowell[1,12], **Jonathan J. Fox**[2,12], **Takao Hashimoto**[2], **Johnny A. Diaz**[2], **Héctor I. Navarro**[1], **Gervaise H. Henry**[3], **Blake A. Feldmar**[2], **Matthew G. Lowe**[1], **Alejandro J. Garcia**[4], **Ye E. Wu**[5,6], **Dipti P. Sajed**[7], **Douglas W. Strand**[3], **Andrew S. Goldstein**[2,8,9,10,11,13,*]

[1]Molecular Biology Interdepartmental Program, University of California, Los Angeles, Los Angeles, CA 90095, USA

[2]Department of Molecular, Cell, and Developmental Biology, University of California, Los Angeles, Los Angeles, CA 90095, USA

[3]Department of Urology, UT Southwestern Medical Center, Dallas, TX 75390, USA

[4]Division of Hematology-Oncology, Department of Medicine, David Geffen School of Medicine, University of California, Los Angeles, Los Angeles, CA 90095, USA

[5]Department of Biological Chemistry, David Geffen School of Medicine, University of California, Los Angeles, Los Angeles, CA 90095, USA

[6]Department of Neurobiology, David Geffen School of Medicine, University of California, Los Angeles, Los Angeles, CA 90095, USA

[7]Department of Pathology and Laboratory Medicine, David Geffen School of Medicine, University of California, Los Angeles, Los Angeles, CA 90095, USA

[8]Department of Urology, David Geffen School of Medicine, University of California, Los Angeles, Los Angeles, CA 90095, USA

[9]Eli and Edythe Broad Center of Regenerative Medicine and Stem Cell Research, University of California, Los Angeles, Los Angeles, CA 90095, USA

[10]Jonsson Comprehensive Cancer Center, University of California, Los Angeles, Los Angeles, CA 90095, USA

[11]Molecular Biology Institute, University of California, Los Angeles, Los Angeles, CA 90095, USA

*Correspondence: agoldstein@mednet.ucla.edu.

[12]These authors contributed equally

AUTHOR CONTRIBUTIONS

P.D.C., J.J.F., T.H., J.A.D., H.I.N., B.A.F., and M.G.L. conducted the experiments. P.D.C., J.J.F., and A.S.G. designed the experiments. P.D.C., J.J.F., and A.S.G. wrote and edited the manuscript. Y.E.W. performed bioinformatics analyses and wrote part of the manuscript. A.J.G. assisted with CyTOF samples and wrote part of the manuscript. D.P.S. provided pathology expertise and wrote part of the manuscript. G.H.H. and D.W.S. performed human prostate experiments and wrote part of the manuscript. A.S.G. procured funding and supervised the experiments.

SUPPLEMENTAL INFORMATION

Supplemental Information can be found online at https://doi.org/10.1016/j.celrep.2019.07.007.

DECLARATION OF INTERESTS

The authors declare no competing interests.

[13]Lead Contact

SUMMARY

Aging is associated with loss of tissue mass and a decline in adult stem cell function in many tissues. In contrast, aging in the prostate is associated with growth-related diseases including benign prostatic hyperplasia (BPH). Surprisingly, the effects of aging on prostate epithelial cells have not been established. Here we find that organoid-forming progenitor activity of mouse prostate basal and luminal cells is maintained with age. This is caused by an age-related expansion of progenitor-like luminal cells that share features with human prostate luminal progenitor cells. The increase in luminal progenitor cells may contribute to greater risk for growth-related disease in the aging prostate. Importantly, we demonstrate expansion of human luminal progenitor cells in BPH. In summary, we define a $Trop2^{+}$ luminal progenitor subset and identify an age-related shift in the luminal compartment of the mouse and human prostate epithelium.

In Brief

Aging is a significant risk factor for BPH and prostate cancer, but how aging increases disease risk in the prostate remains poorly defined. Crowell et al. show that progenitor-enriched luminal cells are expanded with aging in the mouse and human prostate, and may contribute to BPH.

Graphical Abstract

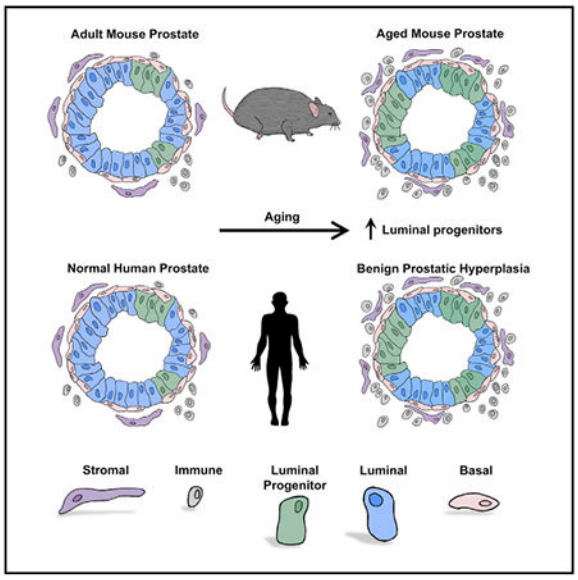

INTRODUCTION

As living organisms age, they experience changes that result in the functional decline of their cells, tissues, and organs, increasing risk for a range of diseases (López-Otín et al., 2013). Many aspects of the aging process are thought to contribute to disease, such as aberrant signaling pathways, defects in autophagy, and shortening of telomeres (Niccoli and Partridge,2012). Aging is associated with a loss of tissue mass, structural integrity, and

regenerative potential (van Deursen, 2014), which may be caused by defects in tissue stem and progenitor cells. Age-related atrophy of muscles, brain, eyes, and thymus has been well documented (Baumgartner et al., 1998; Klein et al., 1992; Meier-Ruge et al., 1992; Simpson et al., 1975), consistent with a decline in progenitor activity in many of these tissues (Conboy et al., 2003; Molofsky et al., 2006). In contrast, the prostate gland has been shown to undergo expansion with age. Prevalence of benign prostatic hyperplasia (BPH), characterized by enlargement of the prostate, increases with age (Roehrborn, 2005). However, the link between age and progenitor capacity in the prostate has not been well defined.

Previous observations in old mice have identified age-related changes in the prostate microenvironment, including stromal disorganization and increased inflammation (Bianchi-Frias et al., 2010). We have previously identified a population of progenitor-like luminal cells in the human prostate that are expanded in regions adjacent to chronic inflammation (Liu et al., 2016). These $CD38^{low}$ luminal progenitor cells express prostate stem cell antigen (PSCA) and exhibit an inflammatory signature. Whether the aging mouse prostate similarly contains a phenotypically distinct subset of progenitor-like luminal cells has not been established.

In this study, we performed transcriptional and functional characterization of epithelial cells from 3-month-old and 24-month-old mice. We found that prostate basal and luminal cells from old mice surprisingly maintain their progenitor activity. Luminal cells from old mice exhibit increased expression of progenitor markers including *Trop2* and *Psca.* Mechanistically, this is driven by an age-related increase in a distinct $Trop2^{+}$ luminal progenitor subset capable of generating large organoids. In human prostate tissues, we found an increase in $PSCA^{+}$ luminal cells associated with age and BPH. Defining the cell types that maintain the prostate with age may shed light on the mechanisms promoting BPH.

RESULTS

Isolation of Prostate Epithelial Cells from Young Adult and Old Mice

We aged C57BL/6 (B6) male mice to 24 months and compared their prostates with post-pubertal 3-month-old young adult mice, hereafter referred to as adult (Figure 1A). Old mouse prostates are heavier than adult prostates (Figure 1B) and contain significantly greater numbers of cells per prostate (Figure 1C). We hypothesized that increased cell number may be caused by increased branching during aging. However, quantification of the number of branch points per lobe (anterior, dorso-lateral, and ventral) did not reveal any statistically significant differences between adult and old prostates (Figures 1D and 1E).

At the histological level, old prostates did not demonstrate features of prostate adenocarcinoma. However, rare agerelated phenotypes were observed. In adult mice, prostatic acini are lined by a cuboidal to columnar epithelium with simple papillary infoldings and uniform nuclei (Figure S1A). In one lobe of an old prostate, acini were observed with a proliferation of the epithelium showing architectural disorganization and increased atypia in the form of nuclear pleomorphism, features of mouse prostatic intraepithelial neoplasia (PIN) (Ittmann et al., 2013) (Figure S1B). We also observed a single

instance of a prostatic lobe with a markedly cellular mesenchymal proliferation infiltrating the space between benign prostatic glands, indicative of malignant sarcomatous features (Figure S1C).

To determine which cell types are responsible for the increased cell number in old prostates, we utilized fluorescence-activated cell sorting (FACS) to distinguish basal, luminal, stromal, and Lin^+ cells (expressing immune and endothelial markers) from adult and old prostates (Figures 1F and 1G). After depleting Lin^+ (CD31, CD45, Ter119) cells, we identified basal and luminal cells based on differential expression of CD49f and epithelial cell adhesion molecules (EpCAM). Intracellular flow cytometry for basal (K14, K5) and luminal (K18, K8) keratins confirmed successful fractionation of basal and luminal cells within the $CD49f^{hi}$ $EpCAM^+$ and $CD49f^{lo}$ $EpCAM^+$ gates, respectively (Figures 1G, S1D, and S1E). Stromal cells, including cells expressing Desmin, were isolated within the Lin^- $CD49f^-$ $EpCAM^-$ fraction (Figures 1G and S1F).

We observed a dramatic increase in the number of Lin^+ cells with age (Figure 1H), consistent with a 3- to 4-fold increase in the proportion of $CD45^+$ cells in old prostates (Figure S1G). We also noted a minor increase in the number of stromal cells in old prostates (Figure 1H). No significant change in the number of basal or luminal epithelial cells was observed. We quantified forward scatter, a feature of FACS that is associated with cell size, from each population of cells. Interestingly, both Lin^+ and stromal cells exhibited a significant decrease in forward scatter levels with age, whereas no significant difference was found in epithelial subsets (Figure 1I). These findings suggest age-related changes in the prostate microenvironment, consistent with a previous report (Bianchi-Frias et al., 2010).

Mass Cytometry Reveals an Age-Related Increase in Prostate-Infiltrating Lymphocytes

Using mass cytometry (cytometry by time-of-flight [CyTOF]) to comprehensively phenotype immune cells, we stained single-cell suspensions of total mouse prostate with a panel of metal-tagged antibodies against cell surface markers (Figure 2A; Table S1). To confirm that CyTOF can accurately detect immune cell populations in the prostate, we compared immune-competent B6 mice and immune-deficient NOD-SCID-IL-R2γ^{null} (NSG) mice that lack T cells, B cells, and natural killer (NK) cells, but still have myeloid cells (Ito et al., 2012). B6 mice were found to have cells staining positive for T cell (CD3, CD4, and CD8), B cell (CD19), and myeloid (CD11b and F4/80) markers (Figure S2A). In contrast, NSG mice stained positively for markers of myeloid cells, but not lymphocytes (Figures S2A–S2C).

We performed CyTOF on FACS-isolated Lin^+ cells from adult and old mouse prostate tissue using the markers CD11c, Ly6C, CD19, CD8, CD25, CD27, B220, CD4, F4/80, CD11b, CD138, CD3, CD117, and FCER1A. To examine age-related changes to the gross immune cell composition of the mouse prostate, we classified $CD45^+$ cells into three major groups. Cells expressing CD3 were classified as T cells. Cells expressing CD19 or B220 were classified as B cells. Cells expressing at least one of the markers, CD11b, CD11c, F4/80, and Ly6C, were classified as myeloid cells. NK and myeloid cells were difficult to separate based on the markers used, so we chose to group them together for this analysis. Although myeloid/NK cells were found to be dominant in both the adult and old mouse prostate

immune compartments, T and B cells significantly increased with age as a proportion of $CD45^+$ cells (Figure 2B).

We used t-Stochastic Neighbor Embedding (t-SNE) to visualize high-dimensional CyTOF data on a two-dimensional scatterplot, where cells with similar expression of surface markers are grouped closer together (Mair et al., 2016). Visualizing the resulting t-SNE plot as a heatmap of marker expression, the T cells and B cells are separated from cells expressing myeloid markers (Figure 2C). Consistent with age-related changes in the proportion of major immune lineages (Figure 2B), T and B cell regions identified in the t-SNE plot appeared more dense in the old mouse prostate (Figure 2D). These results are also consistent with age-related changes in Lin^+ cell size (Figure 1I), because prostate-infiltrating lymphocytes exhibit lower levels of forward scatter than myeloid cells (Figure S2D).

Old Luminal Cells Generate Larger Organoids

Having characterized age-related changes to the prostate microenvironment, we sought to evaluate the effects of aging on prostate epithelial cells. We quantified the percentage of $Ki67^+$ epithelial cells in the mouse prostate by flow cytometry, and found increased proliferation rates in basal cells compared with luminal cells (Figure S3A). Although proliferation rates did not change with age in the basal population, old luminal cells exhibited a significant increase in proliferation rates (Figure S3A). We next utilized the prostate organoid assay (Karthaus et al., 2014) to measure age-related changes in epithelial progenitor activity. We isolated basal and luminal cells from adult and old mice, and measured primary organoid formation, organoid size, and self-renewal capacity upon re-plating into secondary organoid culture. Within the basal cells, no significant age-related differences were observed based on primary organoid-forming capacity (Figure 3A), organoid size (diameter) (Figure 3B), and self-renewal (Figure 3C). Luminal cells from adult and old mice had no significant difference in primary organoid-forming capacity (Figure 3D). Organoids derived from aged luminal cells were larger on average (Figure 3E) and contained a significantly greater proportion of large (>400-μm diameter) organoids than those derived from adult luminal cells (Figure S3B). No significant differences in self-renewal capacity were observed upon re-plating into secondary organoid culture (Figure 3F).

Confocal microscopy was performed to evaluate markers of each lineage in organoids derived from adult and old basal and luminal cells. Basal-derived organoids from both adult and old mice contained multi-layered epithelium with outer layers expressing high levels of the basal marker p63 surrounding inner layers expressing high levels of the luminal marker K8 (Figure 3G). Luminal-derived organoids from both adult and old mice generally contained a single layer of cells with high expression of K8 and low-to-undetectable levels of p63 (Figure 3H). Western blots confirmed expression of basal and luminal markers in organoids derived from each cell type and age, indicative of multipotency (Figures S3C and S3D), as has been reported for adult basal and luminal cells (Chua et al., 2014; Karthaus et al., 2014).

Aging Is Associated with a Luminal Progenitor Signature

To gain insight into age-related changes associated with increased luminal organoid size, we performed gene expression analysis using RNA sequencing (RNA-seq) on epithelial cells isolated from adult and old mouse prostates. Principal component analysis of RNA-seq expression indicated that each cell type and age clusters independently, with principal component (PC) #1 separating basal from luminal cells and PC #2 distinguishing adult from old epithelial cells (Figure 4A). Within each cell type, significant gene expression changes were determined based on greater than 1.5-fold differential expression between adult and old, using a cutoff of false discovery rate (FDR) <0.1. Interestingly, 10 genes were significantly upregulated in both basal and luminal cells from old mice (Figure S4A), including several metabolic genes (*Cyp2f2, Hmox1, Urah*). Fourteen genes were found to be significantly downregulated in both basal and luminal cells from old mice compared with adult mice (Figure S4B), including several genes related to the extracellular matrix (*Col1a1, Col1a2, Col3a1, Sparc*). Reduced expression of collagen genes in old epithelial cells is consistent with a previous report (Bianchi-Frias et al., 2010).

Gene Ontology analysis was performed on gene sets significantly upregulated in each cell type and age, demonstrating that adult basal cells were enriched in terms related to cell adhesion and migration (Figure S4C), whereas the old basal cell signature was associated with ribosome biogenesis (Figure S4D). Within the luminal cells, the adult signature was enriched in male sex differentiation and gonad development (Figure S4E). Several gene ontology terms of interest were enriched in old luminal cells including cell motility and migration, angiogenesis, and inflammatory response (Figure S4F).

A similar signature was previously demonstrated in $CD38^{low}$ luminal progenitor cells in the human prostate (Liu et al., 2016), suggesting that aged mouse prostate luminal cells may share features with human luminal progenitor cells. Several markers of human prostate luminal progenitors, including elevated *Bcl2, Cd74, Pigr*, and *Psca* and low *Cd38*, are associated with aged mouse prostate luminal cells (Figure 4B). Gene set enrichment analysis was used to demonstrate that the aged mouse prostate luminal signature significantly overlaps with the $CD38^{low}$ luminal progenitor signature (Figure 4C).

Elevated Expression of Trop2 in Old Luminal Cells

Old luminal cells were found to express elevated transcript levels of several stem and progenitor cell markers including *Cd44, Itga2*, and *Tacstd2 (Trop2)* (Figure 4B). We performed flow cytometry to measure mean fluorescence intensity (MFI) of Trop2 expression on basal and luminal cells from adult and old mouse prostates. Although Trop2 expression does not change with age on basal cells, old luminal cells express significantly higher levels of Trop2 than adult luminal cells (Figures 4D–4F).

Mechanistically, we wondered whether progenitor genes including *Trop2* are elevated uniformly in old luminal cells or whether there is an age-related expansion of a pre-existing progenitor-like luminal population. By flow cytometry, a subset of luminal cells from both adult and old prostates appeared to express elevated levels of Trop2 (Figure 4F). We utilized immunohistochemistry to evaluate Trop2 expression in adult and old prostate tissue. Trop2

expression was observed on the vast majority of basal cells (Figures 4G and 4H), as well as on proximally located luminal cells in both adult and old prostates, as we have previously reported (Goldstein et al., 2008). In distal regions of adult and old prostates, we observed Trop2-expressing luminal cells in ridges protruding into the lumen of ducts (Figures 4G and 4H), where distally located label-retaining luminal cells were reported to reside (Tsujimura et al., 2002). In old prostates, Trop2-expressing luminal cells were also observed in rare regions with epithelial hyperplasia (Figures 4H and S5).

Trop2 Expression Defines a Subset of Large Organoid-Forming Luminal Progenitor Cells

Using FACS, we isolated a subpopulation of $Trop2^+$ luminal cells from preparations of dissociated adult prostate comprising approximately 5%–6% of total $CD49f^{lo}$ $EpCAM^+$ luminal cells. $Trop2^+$ and $Trop2^-$ luminal cells express comparable levels of the luminal marker K18 and low or absent expression of basal markers K5 and K14 (Figures S6A–S6C). Interestingly, the $Trop2^+$ fraction exhibited a greater proportion of $Ki67^+$ cells (Figure 5A), suggesting that $Trop2^+$ and $Trop2^-$ subsets may be functionally distinct. Upon plating both luminal subpopulations from adult prostate into the organoid-forming assay, we found that $Trop2^+$ luminal cells were capable of forming organoids at a higher rate (Figure 5B). Furthermore, organoids derived from $Trop2^+$ luminal cells were considerably larger than organoids derived from $Trop2^-$ luminal cells (Figure 5C). Both $Trop2^+$ and $Trop2^-$ luminal cells generated organoids containing one or two layers of cells with high expression of K8, whereas $Trop2^+$ luminal-derived organoids tended to express higher levels of p63 than $Trop2^-$ luminal-derived organoids (Figures 5D and 5E). These differences in functional capacity suggest that $Trop2^+$ luminal cells represent a progenitor-enriched subpopulation from the adult prostate.

Age-Related Expansion of $Trop2^+$ Luminal Progenitor Cells

The mean percentage of $Trop2^+$ luminal cells increased from 6% in adult to 21% in old prostates (Figures 5F and 5G), indicating a significant age-related expansion of this subpopulation. Similar fractions of $Trop2^+$ and $Trop2^-$ luminal cells were observed when comparing total dissociated cells and DAPI-negative viable cells (Figures S6D and S6E), ruling out the possibility that the expanded $Trop2^+$ fraction in old prostates is a result of preferential survival during dissociation.

To determine whether luminal subsets defined by Trop2 expression retain their gene signature with age, we performed RNA-seq on $Trop2^+$ and $Trop2^-$ luminal cells from adult and old mice. When comparing genes that were greater than 1.5-fold enriched in $Trop2^+$ luminal cells with a p value <0.05 and FDR < 0.1, we identified 1,121 genes in the adult and 1,252 genes in the old prostate associated with a $Trop2^+$ luminal signature. Importantly, the majority of these genes were shared by both adult (66%) and old (59%) $Trop2^+$ luminal cells (Figure 6A), suggesting an age-related maintenance of the core $Trop2^+$ progenitor signature. Interestingly, the $Trop2^+$ luminal signature includes *Psca* (Figures 6B and 6C), a marker of human prostate luminal progenitor cells (Liu et al., 2016) that was recently shown to define a distinct luminal subset in prostate tissues from healthy human donors (Henry et al., 2018). CD44, a marker of stem and progenitor cells in several epithelial tissues including prostate

(Garraway et al., 2010), was also found in the Trop2$^+$ signature and validated at the protein level by flow cytometry (Figures 6D and 6E).

Similar analysis of genes enriched in Trop2~ luminal cells revealed considerable overlap between adult (61%) and old (41%) prostates (Figure 6A). The degree of overlap within Trop2~ luminal cells was lower than that of Trop2$^+$ luminal cells, which may reflect increased responsiveness to age-related signals from the microenvironment. Alternatively, the Trop2~ luminal subset may contain a greater degree of heterogeneity that has yet to be defined.

Trop2$^+$ Luminal Cells Maintain Progenitor Activity with Age

We evaluated the functional capacity of Trop2$^+$ and Trop2$^-$ luminal cells from both adult and old mice to determine the effect of age on progenitor capacity within each phenotypically defined subset. Both adult and old Trop2$^+$ luminal cells form organoids at similar rates and generate structures of similar size (Figures 6F–6H), indicating an age-related maintenance of the progenitor activity from this subpopulation. In contrast, Trop2$^-$ luminal cells from old prostates have a diminished capacity to form organoids with a trend toward reduced organoid size (Figures 6F–6H). The reduced organoid-forming activity of old Trop2$^-$ luminal cells correlates with a decline in gene expression associated with gene ontology terms cell division, mitotic nuclear division, and cell cycle (Figure 6I).

We multiplied the percentage of luminal cells that are Trop2$^+$ or Trop2$^-$ by the proliferative index (% Ki67$^+$) within each luminal subset to determine the contribution of each subset to total proliferating luminal cells in the mouse prostate. Whereas the majority of proliferating luminal cells in the adult prostate are Trop2$^-$, the majority of proliferating luminal cells in the old prostate express Trop2 (Figure 6J). We quantified the contribution of Trop2$^+$ and Trop2$^-$ cells to total luminal progenitor activity by multiplying the percentage of Trop2$^+$ or Trop2$^-$ luminal cells by the rate of organoid formation for each subset. Whereas 8% of luminal organoids in the young prostate are generated by Trop2$^+$ cells, 64% of luminal organoids in the old prostate arise from Trop2$^+$ progenitor cells (Figure 6K), representing a dramatic age-related shift in the luminal compartment.

Human PSCA$^+$ Luminal Cells and Inflammatory Cells Expand in Aging and BPH

Having demonstrated a significant overlap in gene expression between Trop2$^+$ luminal cells and human luminal progenitor cells, we asked whether luminal progenitor cells are expanded with age in human prostate. Using PSCA as a marker of human prostate luminal progenitor cells (Liu et al., 2016), we evaluated the frequency of PSCA$^+$ luminal cells (Henry et al., 2018) in human prostate tissues from young healthy men and older men with BPH. We observed a significant increase in the percentage of PSCA$^+$ luminal cells in prostates from men with BPH compared with normal prostates from organ donors (Figure 7A). Interestingly, we also found a significant increase in the proportion of CD45$^+$ immune cells in BPH compared with normal prostates (Figure 7B). Both PSCA$^+$ luminal cells and CD45$^+$ immune cells are positively correlated with age in the human prostate (Figures 7C and 7D).

DISCUSSION

Aging is thought to play an important role in the development of BPH and prostate cancer. In this study, we examined the progenitor capacity of the prostate epithelium and found that basal and luminal cells from old mice maintain their organoid-forming activity. Luminal cells from old mice exhibit a progenitor-like signature and generate larger organoids than young adult luminal cells (Figures 3E, 4B, and 4C). We set out to determine whether luminal cells gain progenitor features with age or whether there is an age-related expansion of a pre-existing luminal progenitor subset. We found that Trop2 expression defines a unique subset of luminal cells in the adult prostate that generate large organoids (Figures 4F, 5B, and 5C). The Trop2$^+$ luminal fraction is dramatically expanded with age and contributes to the vast majority of luminal progenitor activity in old mouse prostate (Figures 5F, 5G, and 6K). The age-related expansion of progenitor-like luminal cells was also found in the human prostate in men with BPH (Figure 7A), suggesting that luminal progenitor cells may play a functional role in the disease. In addition to an age-related expansion of luminal progenitor cells, we also found an age-related increase in inflammatory cells in both mouse and human prostates (Figures 7C and 7D). Although mice are not known to develop BPH, our results suggest that further study of mouse prostate aging may reveal mechanisms relevant to BPH.

It remains unclear what mechanisms are responsible for the age-related expansion of Trop2$^+$ luminal cells in the mouse prostate. Basal cells exhibit higher proliferation rates than luminal cells at both 3 and 24 months of age (Figure S3A), consistent with results in the human prostate (Moad et al., 2017). Within the luminal compartment, we observed significantly greater proliferation from the Trop2$^+$ subset in adult mice (Figure 5A). Whether proliferating Trop2$^+$ luminal cells undergo self-renewing divisions or give rise to Trop2$^-$ luminal cells has not been established. An age-related expansion of Trop2$^+$ luminal cells may result from a sustained proliferative advantage within this subset throughout life. Trop2$^+$ luminal cells may also be derived from other epithelial populations, such as basal cells or Trop2$^-$ luminal cells. Lineage tracing will be necessary to distinguish these possibilities.

One possibility is that systemic or local signals originating outside of the epithelium may contribute to the age-related expansion of Trop2$^+$ luminal cells. Given that old mice are heavier than adult mice and contain a greater amount of adipose tissue, we hypothesized that increased body fat in adult mice may replicate the aging phenotype. However, we did not observe an expansion of Trop2$^+$ luminal cells in adult mice fed a high-fat diet for 3 months (Figures S7A–S7F), suggesting that increased body fat in old mice is not likely to drive the luminal progenitor expansion. Changes in hormone levels may play a role in the expansion of Trop2$^+$ luminal cells, as we have previously demonstrated a dramatic increase in Trop2$^+$ luminal cells in the castrated mouse prostate (Goldstein et al., 2008). It remains unclear whether the increase in Trop2$^+$ luminal cells in the castrated prostate arises out of an expansion of pre-existing Trop2$^+$ luminal cells or through the increased expression of Trop2 in castration-resistant luminal cells. Additional studies will be required to define the cues that drive an age-related expansion of luminal progenitor cells.

The age-related expansion of luminal progenitor cells may also increase the risk for prostate cancer initiation. Using a variety of *in vivo* approaches with mouse and human prostate tissue, we and others have established that progenitor cells within both the basal and the luminal layers are capable of initiating prostate cancer in response to genetic alterations (Choi et al., 2012; Goldstein et al., 2008, 2010; Kwon et al., 2014; Lawson et al., 2010; Lu et al., 2013; Park et al., 2016; Stoyanova et al., 2013; Wang et al., 2009, 2013). Therefore, as luminal progenitor cells expand with age in the prostate, the pool of potential target cells for transformation likely expands as well. Future work will be aimed at determining whether aged prostate epithelial cells are more susceptible to oncogenic transformation.

STAR★METHODS

LEAD CONTACT AND MATERIALS AVAILABILITY

This study did not generate new unique reagents. Further information and requests for resources and reagents should be directed to and will be fulfilled by the Lead Contact, Andrew S. Goldstein (agoldstein@mednet.ucla.edu).

EXPERIMENTAL MODEL AND SUBJECT DETAILS

Animal Work—Immunocompetent male C57BL/6J and C57BL/6N mice (B6) and immunodeficient male NOD.Cg-*Prkdc*^{scid} *Il2rg*^{tm1Wjl} (NSG) mice from Jackson Laboratories and the UCLA Department of Radiation Oncology's animal core facility were used in experiments. Mice were bred and maintained under the care of the UCLA Division of Laboratory Animal Medicine (DLAM), using approved protocols. For aging experiments, mice were purchased from Jackson Laboratories at 12 months of age and were maintained at UCLA until they reached 24 months of age. For high fat diet experiments, 4 week-old B6 mice were fed normal chow or high fat diet (58Y1, Test Diet) for 14 weeks.

Collection of Mouse Prostate Tissue—Male mice were euthanized using carbon dioxide asphyxiation, and the urogenital tract was removed and placed into RPMI 1640 (GIBCO) containing 10% fetal bovine serum (FBS) (Corning), 1x penicillin-streptomycin (GIBCO). Under a microscope, seminal vesicles, the bladder, the urethra, and fat were removed from the urogenital tract to isolate the prostate. Mouse prostates were weighed, and weights were recorded.

Collection of Human Prostate Tissue—Prostate specimens used in this study were obtained from 10, 18-47 year old male organ donors whose families were consented at the Southwest Transplant Alliance from March 2017 to April 2019 under IRB STU 112014-033. After transplantable organs were harvested, a cystoprostatectomy was performed and the specimen was transported to UT Southwestern Medical Center for processing. Ten aged prostate specimens were collected from patients undergoing simple prostatectomy at Clements University Hospital for lower urinary tract symptoms due to BPH from March 2018 to April 2019 under IRB STU 112014-033.

METHOD DETAILS

Quantification of Branch Points—Branch point of mouse prostate lobes was quantified as described (Lai et al., 2012) with modifications. Briefly, the mouse prostate lobes were dissected and digested with 10 mg/ml collagenase type I (GIBCO) in RPMI 1640 (GIBCO) with 10% fetal bovine serum (Corning) for 1 h at 37°C. The ductal structure was exposed with fine forceps and branching points were counted under a dissection microscope.

Mouse Prostate Dissociation to Single Cells—Using a razor blade, individual mouse prostates were mechanically dissociated in dissociation media comprised of RPMI 1640 (GIBCO) containing 10% fetal bovine serum (Corning), 1x penicillin-streptomycin (GIBCO), 1 mg/mL collagenase type I (GIBCO), 1 mg/ml dispase (GIBCO), 0.1 mg/mL deoxyribonuclease (GIBCO), and 10uM of the p160ROCK inhibitor Y-27632 dihydrochloride (Tocris Bioscience). When chunks were no longer visible, the samples were incubated at 37°C on a nutating platform for 1 - 1.5 h in 5 mL of dissociation media. After centrifugation, the pellet was washed with 1x phosphate buffered saline (PBS, GIBCO). The cell pellet was resuspended in 2.7 mL of 0.05% Trypsin-EDTA (GIBCO) and incubated at 37°C for 5 min. Trypsin was inactivated with 300 μL of dissociation media. Cells were further dissociated by pipetting with a P-1000 pipette and an 18G syringe. Cells were passed through a 100 μm cell strainer (Corning). Dissociated cells were counted using a hemocytometer.

Human Prostate Processing—Fresh tissue samples less than 24 h post-collection were transported in ice-cold saline and immediately processed in a 4 h enzymatic digestion into single cells at 37°C using 5 mg/ml collagenase type I (GIBCO), 10 μM ROCK inhibitor Y-27632 (Tocris Bioscience), 1nM DHT (Sigma), 1mg DNase I (GIBCO), and 1% antibiotic/antimycotic solution (100X, Corning) in HBSS. Single cells were filtered and cryopreserved in 90% FBS/10% DMSO. For experiments, vials were rapidly thawed, washed, and incubated with antibodies for flow cytometry as described (Henry et al., 2018). Viable human prostate cells were analyzed by fluorescence activated cell sorting in the UT Southwestern CRI Flow Cytometry Core on a BD FACSAria FUSION SORP flow cytometer and analyzed with FlowJo software as performed previously (Henry et al., 2018).

Staining and Sorting Cells from Mouse Prostate—Dissociated cells were stained with directly conjugated primary antibodies: rat anti-CD49f-PE (BioLegend), rat anti-CD326 (EpCAM)-APC/Cy7 (BioLegend), goat anti-Trop2-APC (R &D Systems), rat anti-CD31-FITC (BioLegend), rat anti-CD45-FITC (BioLegend), and rat anti-Ter119-FITC (BioLegend) for 20 min on ice. Rat anti-ESAM-FITC (BioLegend) was also added to the Lin panel for some experiments. Rat anti-CD44-FITC (BioLegend) was used for analysis. Cells were stained in media containing RPM11640 (GIBCO), 10% FBS (Corning), 1x penicillin-streptomycin (GIBCO), and 10uM of the p160ROCK inhibitor Y-27632 dihydrochloride (Tocris Bioscience). Sorting was performed on a BD FACS Aria II (BD Biosciences) and flow cytometry analysis was performed on a BD FACS Canto (BD Biosciences).

Intracellular Flow Cytometry—Dissociated cells from mouse prostate were stained with rat anti-CD49f-PE (BioLegend), rat anti-CD326 (EpCAM)-APC/Cy7 (BioLegend) and goat anti-Trop2-APC (R & D Systems) for 20 min on ice. Cells were washed with PBS and fixed in 1ml of 2% paraformaldehyde made from 16% paraformaldehyde (Electron Microscopy Sciences) in PBS for 15 min on ice. Cells were washed with PBS and permeabilized in 1ml of permeabilization buffer (0.1% Saponin (Sigma-Aldrich), 5% FBS (Corning) in PBS) for 15 min at room temperature in the dark. Cells were resuspended in 100 μL of permeabilization buffer and stained with either rabbit anti-cytokeratin 5-Alexa Fluor 647 (Abcam) and rabbit anti-cytokeratin 8-Alexa Fluor 488 (Abcam), mouse anti-cytokeratin 14-FITC (Abcam), mouse anti-cytokeratin 18-FITC (Abcam) or rat anti-Ki67-FITC (BioLegend) for 20 min at room temperature in the dark. Cells were washed and resuspended in permeabilization buffer for analysis on a BD FACS Canto (BD Biosciences).

Organoid Culture and Assays—Basal and luminal primary cells from mouse prostate were isolated by fluorescence activated cell sorting. Luminal cell populations were double-sorted to ensure high purity. Sorted cell populations were plated in a 24-well plate (Corning). Basal cells were plated at a density of 500 or 1000 cells/well, while luminal cells were plated at a density of 2500 or 5000 cells/well. Prostate organoids were cultured based on established protocols (Drost et al., 2016). For passaging, primary organoids were dissociated in 1mg/ml dispase (GIBCO) for 30 min to 1 h prior to treatment with 0.05% Trypsin-EDTA (GIBCO) and re-plating. Single organoids were imaged on a light microscope and organoid diameter was measured as a readout of organoid size. For confocal microscopy, dispase-treated organoids were fixed with 4% paraformaldehyde in PBS for 2 h at room temperature, and permeabilized by incubating in blocking solution (10% fetal bovine serum and 0.2% Triton X-100 (Fisher) in PBS) for 2 h. Whole-mount immunofluorescent staining of organoids was performed by incubating with primary antibodies in blocking solution overnight at 4°C, washing with PBS three times for two h each, incubating with secondary antibodies and 1 μg/ml 4’,6-diamidino-2-phenylindole dihydrochloride (DAPI, Sigma) in blocking solution overnight at 4°C, and washing with PBS three times for two h each. Tissue clearing was done with sucrose series (15%, 30%, 45%, and 60% sucrose with 1% Triton X-100 (Fisher) in PBS, 2 h each), and the organoids were mounted on chambered coverslips (35 mm micro-dish, Ibidi USA). Confocal microscopy with Airyscan was performed with LSM 880 (Zeiss). Primary antibodies used were rabbit anti-p63 (BioLegend) and mouse anti-K8 (BioLegend). Secondary antibodies used were Alexa Fluor 488 goat antimouse IgG (Invitrogen) and Alexa Fluor 594 goat anti-rabbit IgG.

Immunoblot Analysis—Organoids were collected at day 7 and lysed in RIPA buffer (50mM Tris-HCl pH 8.0, 150mM NaCl, 1% NP-40, 0.5% Sodium Deoxycholate, 0.1% SDS) containing a complete protease inhibitor cocktail tablet (Roche) and every sample was sonicated with sonic dismembrator (Fisher). Proteins were run on NuPAGE 4%–12% Bis-Tris Gel (Novex) and transferred onto PVDF membranes (Millipore Sigma) and probed with antibodies. Keratin 5 and tubulin were detected via fluorescence using goat anti-rabbit IgG-Alexa Fluor 647 (Invitrogen) or goat anti-mouse IgG-Alexa Fluor 647 (Invitrogen) and all others using HRP-conjugated antibodies against rabbit, mouse, or goat IgG (Invitrogen).

Immunoblot antibodies: rabbit anti-keratin 5 (Biolegend), goat anti-Tp63 (R & D systems), mouse anti-cytokeratin 8 (Biolegend), rabbit anti-Prom1 (Abnova), mouse anti-tubulin (DSHB).

Immunohistochemistry—3-month-old and 24-month-old mouse prostate tissue was embedded in paraffin and sectioned at UCLA's Translational Pathology Core Laboratory. Sections were incubated at 60°C in a vacuum oven for 45-60 min. Slides were transferred into xylene (Fisher) 3 times, 100% alcohol (Decon Labs) 2 times, 95% ethanol 1 time and 70% ethanol 1 time, each for 3 min. Slides were transferred into PBS (GIBCO) for 5 min prior to epitope unmasking using a heat antigen retrieval step. Staining of sections was performed using the manufacturer's protocol for the Anti-Goat HRP-DAB Cell & Tissue Staining Kit (R & D Systems) with primary antibody goat antimouse Trop2 (R & D Systems) at a 10 μg/ml concentration. Hematoxylin and eosin staining was performed by UCLA's Translational Pathology Core Laboratories. Frozen sections were fixed with 4% paraformaldehyde in PBS for 5 min at room temperature, washed with PBS, and stained with primary antibodies and stained with the following secondary antibodies: goat anti-mouse IgG-Alexa Fluor 488 and goat anti-rabbit IgG-Alexa Fluor 594.

Antibodies for Mass Cytometry—Antibodies used for mass cytometry experiments were purchased pre-conjugated from the manufacturer (Fluidigm) or conjugated inhouse using MaxPar X8® multimetal labeling kit (Fluidigm) according to manufacturer's protocol. Panels were checked for signal tolerance using the Maxpar Panel Designer (Fluidigm). Table S1 shows the antibodies used in the mouse panel.

Cell Surface Staining for Mass Cytometry—Cell staining buffer was prepared with 1x PBS (GIBCO) containing 5% bovine serum albumin (BSA) protease-free (Sigma-Aldrich) and 0.2% sodium azide (Sigma-Aldrich). From single-cell suspension into tubes, $1 \times 10^5 - 1.5 \times 10^5$ cells were aliquoted for the unstained control, and $3 \times 10^5 - 1.8 \times 10^6$ cells aliquoted used for the stained samples. For Live/Dead staining with rhodium, samples were centrifuged and resuspended at 1×10^6 cells/mL in cell staining buffer containing 1 μM Cell-ID Intercalator-103Rh (Fluidigm) and incubated at 37°C for 15 min. For Live/Dead staining with cisplatin, samples were centrifuged and resuspended at 1×10^7 cells/mL in cell staining buffer. Stock Cell-ID Cisplatin (Fluidigm) was added to samples for a final concentration of 5 μM, and samples were incubated for 5 min at room temperature. Live/Dead stain was quenched with 2mL cell staining buffer and centrifuged. After Live/Dead staining, the antibody cocktail prepared was diluted to 1 μL of each antibody per 50 μL per sample. Cells were resuspended in 45 μL cell staining buffer and 5 μL of 5 μg/mL TruStain fcX (anti-mouse CD16/32) Antibody (BioLegend). Samples were incubated at room temperature for 10 min, then 50 μL of the antibody cocktail was added. Samples were incubated with antibodies added at room temperature for 30 min then washed twice with cell staining buffer and resuspended in 1 mL Maxpar® Fix and Perm Buffer (Fluidigm) containing 125 nM Cell-ID Intercalator-Ir (Fluidigm). Samples were incubated for 12 – 48 h at 4°C. Samples were then washed a total of 3 times with cell staining buffer, 1x PBS (GIBCO), then MilliQ Water (Millipore). Samples were passed through a 40 mm strainer

(Corning) between the PBS and MilliQ Water washes. After the final wash, cells were resuspended in a residual amount of MilliQ Water for mass cytometry.

Mass Cytometry—Mass cytometry was performed at the UCLA Jonsson Comprehensive Cancer Center (JCCC) and Center for AIDS Research Flow Cytometry Core Facility. Prior to sample introduction cell pellets were washed twice with Maxpar® cell staining buffer (Fluidigm), twice with MilliQ Water and resuspended in 10% EQ Four Element Calibration Beads (Fluidigm) containing natural abundance cerium (140/142Ce), europium (151/153Eu), holmium (165Ho), and lutetium (175/176Lu). Samples were acquired on a Helios® mass cytometer (Fluidigm) at an event rate of 300-500 events/second. Post-acquisition data was normalized using bead-based normalization in the CyTOF software.

RNaseq—RNA was extracted from the cells using the RNeasy Mini Kit (QIAGEN) following the manufactural instruction. Libraries for RNA-Seq were prepared with KAPA Stranded mRNA-Seq Kit (Roche). The workflow consists of mRNA enrichment, cDNA generation, and end repair to generate blunt ends, A-tailing, adaptor ligation and PCR amplification. Different adaptors were used for multiplexing samples in one lane. Sequencing was performed on Illumina HiSeq 3000 for 1×50 run.

QUANTIFICATION AND STATISTICAL ANALYSIS

RNaseq Analysis—Data quality check was done on Illumina Sequence Analysis Viewer (SAV). Demultiplexing was performed with Illumina Bcl2fastq2 v 2.17 program. The reads were first mapped to the latest UCSC transcript set using Bowtie2 version 2.1.0 (Langmead and Salzberg, 2012) and the gene expression level was estimated using RNA-seq by Expectation-Maximization (RSEM) v1.2.15 (Li and Dewey, 2011). TMM (trimmed mean of M values) was used to normalize the gene expression. Differentially expressed genes were identified using the Empirical Analysis of Digital Gene Expression Data in R (edgeR) program (Robinson et al., 2010). Genes showing altered expression with $p < 0.05$, FDR <0.1 and more than 1.5 fold changes were considered differentially expressed. Gene ontology analysis was performed using the R package goseq (Young et al., 2010), with gene length corrected. Up- and downregulated genes were separately tested and all genes that were detected (read count > 0) in at least two samples were used as the background. Gene ontology terms with p value < 0.05 were considered statistically significant. Gene ontology analysis was also performed using DAVID Bioinformatics (Huang et al., 2009). Heatmap of candidate genes was generated using the heatmap.2 function in the R package gplots. Expression values were scaled for each row (gene). GSEA analysis was performed using the GSEA software (https://www.broadinstitute.org/gsea) (Subramanian et al., 2005). Normalized enrichment score and false discovery rate were calculated.

CyTOF Clustering—Manual gating for live $CD45^+$ singlets in each sample was performed in FlowJo V10 (FlowJo LLC). Each sample was given a unique Sample ID, then all samples were concatenated into a single .fcs file. On this file T-Distributed Stochastic Neighbor Embedding (t-SNE) in FlowJo V10 was performed on equal numbers of cells from 3- and 24-month-old mouse prostate using all surface markers besides CD45 and the following

settings: Iterations, 3000; Perplexity, 50; Eta (learning rate), 4105. Heatmaps of marker expression were generated using the Color Map Axis function.

Statistical Analysis—Prism V7 (GraphPad) was used to generate graphs and perform statistical analysis. Correlations were determined by calculating the Pearson correlation coefficient r. Number of replicates, type of replicate, and type of error bars are listed in figure legends. Unless otherwise stated, two-tailed Student's t test assuming unequal variance was performed to determine statistical significance. *$p < 0.05$, **$p < 0.01$, ***$p < 0.001$, ****$p < 0.0001$.

DATA AND CODE AVAILABILITY

The data discussed in this publication have been deposited in NCBI's Gene Expression Omnibus and are accessible through GEO Series accession number GSE122367 and GSE128724.

Supplementary Material

Refer to Web version on PubMed Central for supplementary material.

ACKNOWLEDGMENTS

We thank the families of organ donors at the Southwest Transplant Alliance for their commitment to basic science research. Special thanks to Donghui Cheng for cell sorting, Jack Mottahedeh for mouse work, Tom Carmichael and Stacey Gallegos for aged mice, Enca Montecino-Rodriguez and Ken Dorshkind for high-fat-diet mice, and Miriam Guemes for CyTOF sample acquisition. Mass cytometry was performed in the UCLA Jonsson Comprehensive Cancer Center (JCCC) and Center for AIDS Research Flow Cytometry Core Facility that is supported by NIH awards P30 CA016042 and 5P30 AI028697. The purchase of the Helios/CyTOF mass cytometer that was used in this work was, in part, supported by funds provided by the James B. Pendleton Charitable Trust. J.J.F. is supported by a scholarship from the UCLA Minor in Biomedical Research and the Silva Endowment as part of the Undergraduate Research Scholars Program at UCLA. P.D.C. and M.G.L. are supported by the Ruth L. Kirschstein National Research Service Award GM007185. H.I.N. is supported by the Eugene V. Cota-Robles Fellowship. J.A.D. is supported by the National Institute of General Medical Sciences of the NIH (R25GM055052 awarded to T. Hasson) and the Saul Martinez Scholarship. A.S.G. is supported by the Spitzer Family Foundation Fund and the Gill Endowment. This work was supported by the American Cancer Society (RSG-17-068-01-TBG), Department of Defense (W81XWH-13-1-0470), Margaret E. Early Medical Research Trust, STOP CANCER, NIH/NCI {P50CA092131/UCLA SPORE in Prostate Cancer), UCLA Eli and Edythe Broad Center of Regenerative Medicine and Stem Cell Research Rose Hills Foundation Innovator Grant, and support from UCLA's Jonsson Comprehensive Cancer Center, Broad Stem Cell Research Center, Clinical and Translational Science Institute, and Institute of Urologic Oncology. D.W.S. is supported by the NIH/NIDDK (R01 DK115477). We thank UCLA's Technology Center for Genomics and Bioinformatics, Translational Pathology Core Laboratories, and UCLA's Institute for Quantitative and Computational Biology. The anti-alpha-tubulin monoclonal antibody (12G10) was obtained from the Developmental Studies Hybridoma Bank, created by the NICHD of the NIH and maintained at the University of Iowa, Department of Biology, Iowa City, IA.

REFERENCES

Baumgartner RN, Koehler KM, Gallagher D, Romero L, Heymsfield SB, Ross RR, Garry PJ, and Lindeman RD (1998). Epidemiology of sarcopenia among the elderly in New Mexico. Am. J. Epidemiol 147, 755–763. [PubMed: 9554417]

Bianchi-Frias D, Vakar-Lopez F, Coleman IM, Plymate SR, Reed MJ, and Nelson PS (2010). The effects of aging on the molecular and cellular composition of the prostate microenvironment. PLoS ONE 5, e12501. [PubMed: 20824135]

Choi N, Zhang B, Zhang L, Ittmann M, and Xin L (2012). Adult murine prostate basal and luminal cellsare self-sustained lineagesthat can both serve as targets for prostate cancer initiation. Cancer Cell 21, 253–265. [PubMed: 22340597]

Chua CW, Shibata M, Lei M, Toivanen R, Barlow LJ, Bergren SK, Badani KK, McKiernan JM, Benson MC, Hibshoosh H, and Shen MM (2014). Single luminal epithelial progenitors can generate prostate organoids in culture. Nat. Cell Biol 16, 951–961, 1–4. [PubMed: 25241035]

Conboy IM, Conboy MJ, Smythe GM, and Rando TA (2003). Notch-mediated restoration of regenerative potential to aged muscle. Science 302, 1575–1577. [PubMed: 14645852]

Drost J, Karthaus WR, Gao D, Driehuis E, Sawyers CL, Chen Y, and Clevers H (2016). Organoid culture systemsforprostate epithelial and cancer tissue. Nat. Protoc 11, 347–358. [PubMed: 26797458]

Garraway IP, Sun W, Tran CP, Perner S, Zhang B, Goldstein AS, Hahm SA, Haider M, Head CS, Reiter RE, et al. (2010). Human prostate sphere-forming cells represent a subset of basal epithelial cells capable of glandular regeneration in vivo. Prostate 70, 491–501. [PubMed: 19938015]

Goldstein AS, Lawson DA, Cheng D, Sun W, Garraway IP, and Witte ON (2008). Trop2 identifies a subpopulation of murine and human prostate basal cells with stem cell characteristics. Proc. Natl. Acad. Sci. USA 105, 20882–20887. [PubMed: 19088204]

Goldstein AS, Huang J, Guo C, Garraway IP, and Witte ON (2010). Identification of a cell of origin for human prostate cancer. Science 329, 568–571. [PubMed: 20671189]

Henry GH, Malewska A, Joseph DB, Malladi VS, Lee J, Torrealba J, Mauck RJ, Gahan JC, Raj GV, Roehrborn CG, et al. (2018). A Cellular Anatomy of the Normal Adult Human Prostate and Prostatic Urethra. Cell Rep. 25, 3530–3542.e5. [PubMed: 30566875]

Huang W, Sherman BT, and Lempicki RA (2009). Systematic and integrative analysis of large gene lists using DAVID bioinformatics resources. Nat. Protoc 4, 44–57. [PubMed: 19131956]

Ito R, Takahashi T, Katano I, and Ito M (2012). Current advances in humanized mouse models. Cell. Mol. Immunol 9, 208–214. [PubMed: 22327211]

Ittmann M, Huang J, Radaelli E, Martin P, Signoretti S, Sullivan R, Simons BW, Ward JM, Robinson BD, Chu GC, et al. (2013). Animal models of human prostate cancer: the consensus report of the New York meeting ofthe Mouse ModelsofHuman Cancers Consortium Prostate Pathology Committee. Cancer Res. 73, 2718–2736. [PubMed: 23610450]

Karthaus WR, Iaquinta PJ, Drost J, Gracanin A, van Boxtel R, Wongvipat J, Dowling CM, Gao D, Begthel H, Sachs N, et al. (2014). Identification of multipotent luminal progenitor cells in human prostate organoid cultures. Cell 759, 163–175.

Klein R, Klein BE, and Linton KL (1992). Prevalence of age-related maculopathy. The Beaver Dam Eye Study. Ophthalmology 99, 933–943. [PubMed: 1630784]

Kwon OJ, Zhang L, Ittmann MM, and Xin L (2014). Prostatic inflammation enhances basal-to-luminal differentiation and accelerates initiation of prostate cancer with a basal cell origin. Proc. Natl. Acad. Sci. USA 777, E592–E600.

Lai KP, Yamashita S, Vitkus S, Shyr CR, Yeh S, and Chang C (2012). Suppressed prostateepithelial developmentwith impaired branching morphogenesis in mice lacking stromal fibromuscular androgen receptor. Mol. Endocrinol 26, 52–66. [PubMed: 22135068]

Langmead B, and Salzberg SL (2012). Fast gapped-read alignment with Bowtie 2. Nat. Methods 9, 357–359. [PubMed: 22388286]

Lawson DA, Zong Y, Memarzadeh S, Xin L, Huang J, and Witte ON (2010). Basal epithelial stem cells are efficient targets for prostate cancer initiation. Proc. Natl. Acad. Sci. USA 707, 2610–2615.

Li B, and Dewey CN (2011). RSEM: accurate transcript quantification from RNA-Seq data with or without a reference genome. BMC Bioinformatics 72, 323.

Liu X, Grogan TR, Hieronymus H, Hashimoto T, Mottahedeh J, Cheng D, Zhang L, Huang K, Stoyanova T, Park JW, et al. (2016). Low CD38 Identifies Progenitor-like Inflammation-Associated Luminal Cells that Can Initiate Human Prostate Cancer and Predict Poor Outcome. Cell Rep. 77, 2596–2606.

López-Otín C, Blasco MA, Partridge L, Serrano M, and Kroemer G (2013). The hallmarks ofaging. Cell 753, 1194–1217.

Lu TL, Huang YF, You LR, Chao NC, Su FY, Chang JL, and Chen CM (2013). Conditionallyablated Pten in prostate basal cells promotes basal-to-luminal differentiation and causes invasive prostate cancer in mice. Am. J. Pathol 182, 975–991. [PubMed: 23313138]

Mair F, Hartmann FJ, Mrdjen D, Tosevski V, Krieg C, and Becher B (2016). The end of gating? An introduction to automated analysis of high dimensional cytometry data. Eur. J. Immunol 46, 34–43. [PubMed: 26548301]

Meier-Ruge W, Ulrich J, Bruhlmann M, and Meier E (1992). Age-related white matter atrophy in the human brain. Ann. N Y Acad. Sci 673, 260–269. [PubMed: 1485724]

Moad M, Hannezo E, Buczacki SJ, Wilson L, El-Sherif A, Sims D, Pickard R, Wright NA, Williamson SC, Turnbull DM, et al. (2017). Multipotent Basal Stem Cells, Maintained in Localized Proximal Niches, Support Directed Long-Ranging Epithelial Flows in Human Prostates. Cell Rep. 20, 1609–1622. [PubMed: 28813673]

Molofsky AV, Slutsky SG, Joseph NM, He S, Pardal R, Krishnamurthy J, Sharpless NE, and Morrison SJ (2006). Increasing p16INK4a expression decreases forebrain progenitors and neurogenesis during ageing. Nature 443, 448–452. [PubMed: 16957738]

Niccoli T, and Partridge L (2012). Ageing as a risk factor for disease. Curr. Biol 22, R741–R752. [PubMed: 22975005]

Park JW, Lee JK, Phillips JW, Huang P, Cheng D, Huang J, and Witte ON (2016). Prostate epithelial cell of origin determines cancer differentiation state in an organoid transformation assay. Proc. Natl. Acad. Sci. USA 773, 4482–4487.

Robinson MD, McCarthy DJ, and Smyth GK (2010). edgeR: a Bioconductor package for differential expression analysis of digital gene expression data. Bioinformatics 26, 139–140. [PubMed: 19910308]

Roehrborn CG (2005). Benign prostatic hyperplasia: an overview. Rev. Urol 7 (Suppl 9), S3–S14.

Simpson JG, Gray ES, and Beck JS (1975). Age involution in the normal human adult thymus. Clin. Exp. Immunol 79, 261–265.

Stoyanova T, Cooper AR, Drake JM, Liu X, Armstrong AJ, Pienta KJ, Zhang H, Kohn DB, Huang J, Witte ON, and Goldstein AS (2013). Prostate cancer originating in basal cells progresses to adenocarcinoma propagated by luminal-like cells. Proc. Natl. Acad. Sci. USA 110, 20111–20116. [PubMed: 24282295]

Subramanian A, Tamayo P, Mootha VK, Mukherjee S, Ebert BL, Gillette MA, Paulovich A, Pomeroy SL, Golub TR, Lander ES, and Mesirov JP (2005). Gene set enrichment analysis: a knowledge-based approach for interpreting genome-wide expression profiles. Proc. Natl. Acad. Sci. USA 102, 15545–15550. [PubMed: 16199517]

Tsujimura A, Koikawa Y, Salm S, Takao T, Coetzee S, Moscatelli D, Shapiro E, Lepor H, Sun TT, and Wilson EL (2002). Proximal location of mouse prostate epithelial stem cells: a model of prostatic homeostasis. J. Cell Biol 157, 1257–1265. [PubMed: 12082083]

van Deursen JM (2014). The role of senescent cells in ageing. Nature 509, 439–446. [PubMed: 24848057]

Wang X, Kruithof-de Julio M, Economides KD, Walker D, Yu H, Halili MV, Hu YP, Price SM, Abate-Shen C, and Shen MM (2009). A luminal epithelial stem cell that is a cell of origin for prostate cancer. Nature 461, 495–500. [PubMed: 19741607]

Wang ZA, Mitrofanova A, Bergren SK, Abate-Shen C, Cardiff RD, Califano A, and Shen MM (2013). Lineage analysis of basal epithelial cells reveals their unexpected plasticity and supports a cell-of-origin model for prostate cancer heterogeneity. Nat. Cell Biol 15, 274–283. [PubMed: 23434823]

Young MD, Wakefield MJ, Smyth GK, and Oshlack A (2010). Gene ontology analysis for RNA-seq: accounting for selection bias. Genome Biol. 11, R14. [PubMed: 20132535]

Highlights

- Organoid-forming capacity is maintained in old mouse prostate epithelial cells
- Identification of Trop2^{+} luminal cells as a progenitor-enriched subset
- Trop2^{+} luminal progenitor cells are expanded in the aging mouse prostate
- Increase in PSCA^{+} luminal progenitor cells in aging human prostate and BPH

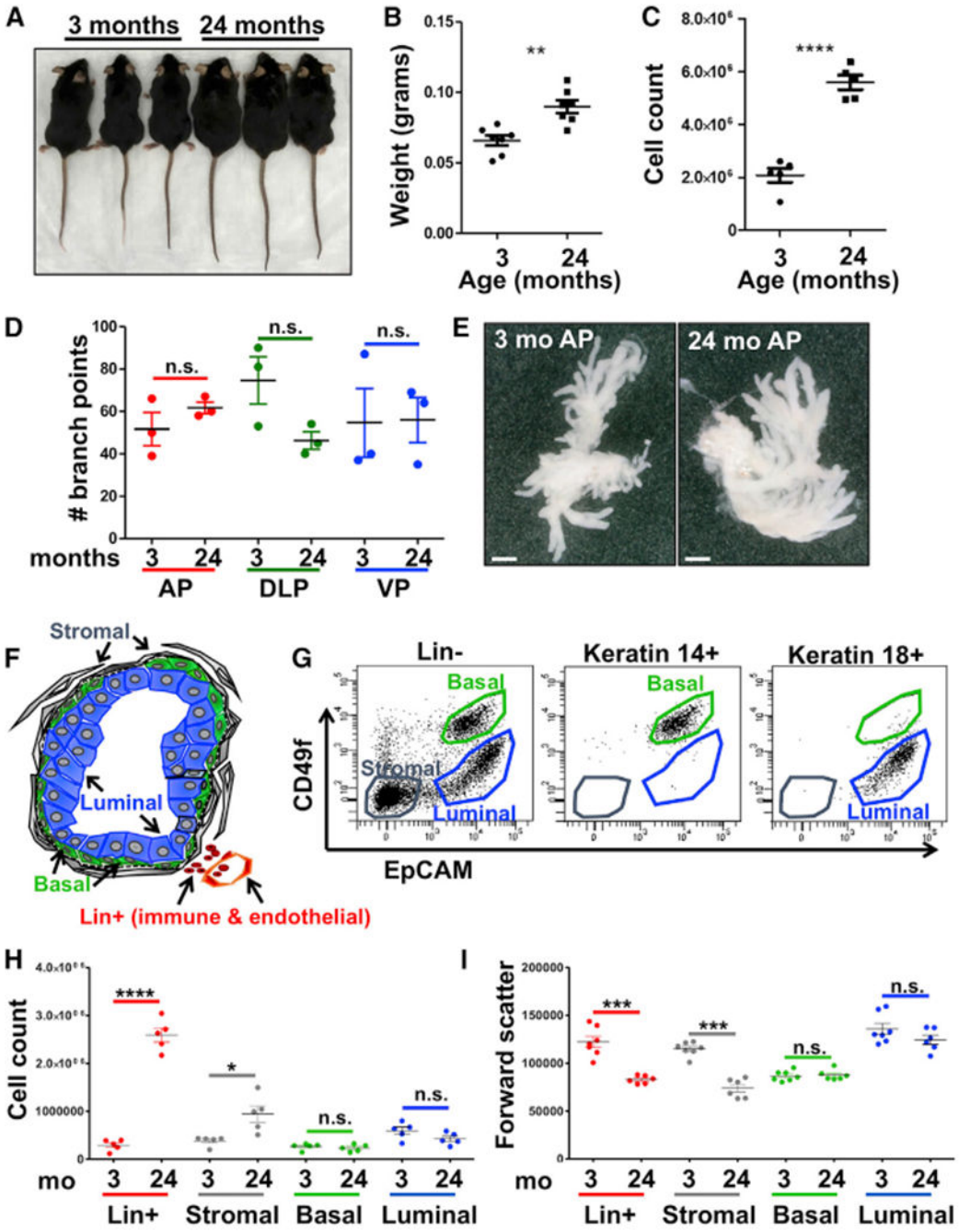

Figure 1. Characterization of Adult and Old Mouse Prostates

(A) Representative images of adult (3-month-old) and old (24-month-old) mice.

(B) Weights of prostates isolated from adult and old mice.

(C) Number of dissociated cells per prostate from each age.

(D) Quantification of the number of branch points in the anterior prostate (AP), dorso-lateral prostate (DLP), and ventral prostate (VP) lobes isolated from adult and old mice.

(E) Representative images of branching in AP lobe of adult and old prostate. Scale bars, 1 mm.

(F) Illustration of the normal mouse prostate gland, including basal cells (green), luminal cells (blue), stromal cells (gray), and Lin^+ immune and endothelial cells (red). Basement membrane is shown as a dotted line.

(G) Fluorescence-activated cell sorting (FACS) of whole mouse prostate using surface antibodies (CD49f and EpCAM) and intracellular staining to identify basal and luminal populations. Left: gated on total Lin^- cells. Center: gated on $K14^+$ basal cells. Right: gated on $K18^+$ luminal cells.

(H and I) Quantification of the number (H) and forward scatter (I) of Lin^+, stromal, basal, and luminal cells in mouse prostates at 3 and 24 months of age. Data represent mean ± SEM of five to seven biological replicates.

Lin, lineage (CD31, CD45, Ter119); Mo, months of age. *$p < 0.05$, **$p < 0.01$, ***$p < 0.001$, ****$p < 0.0001$. n.s. = not significant, $p \geq 0.05$.

See also Figure S1.

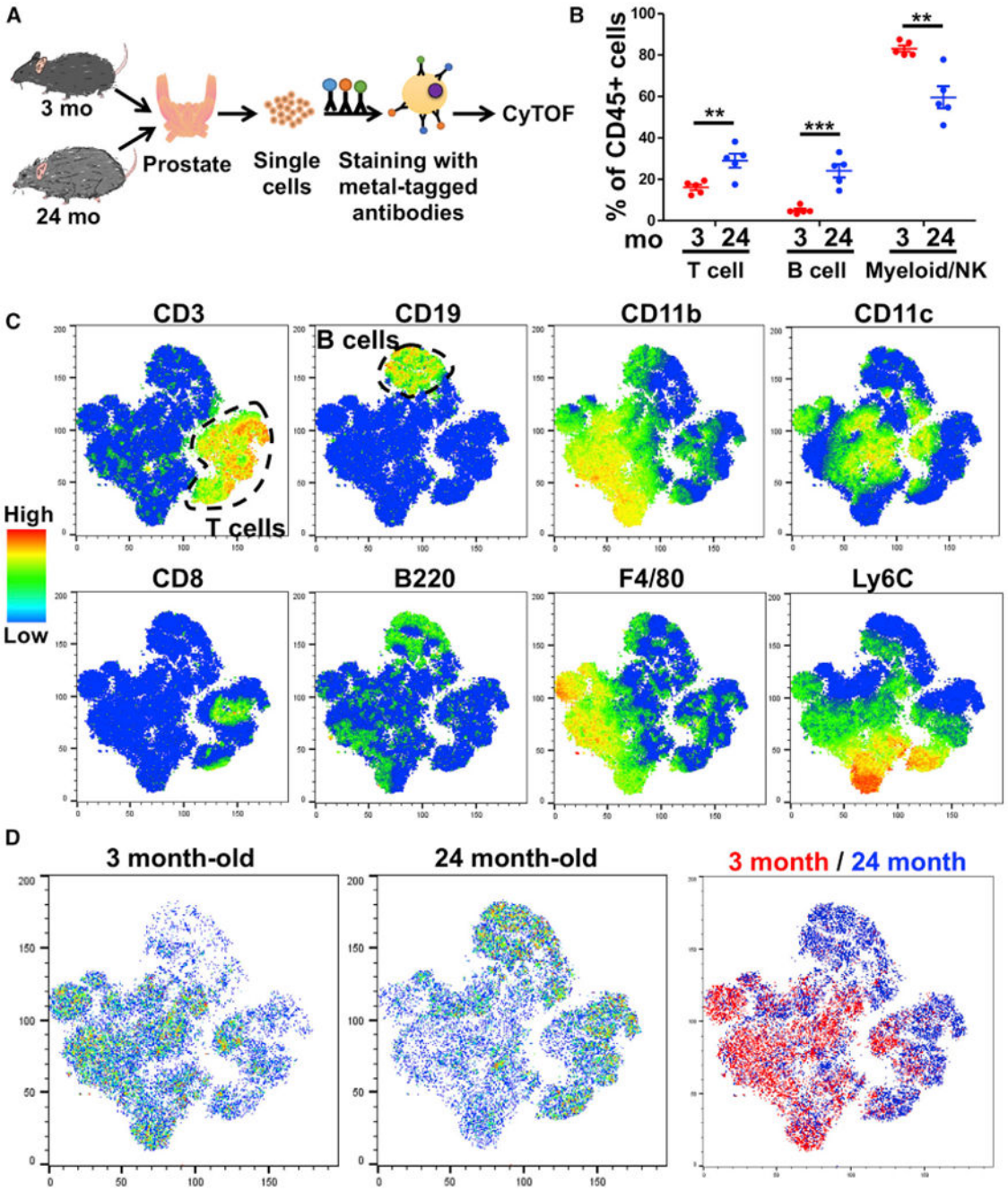

Figure 2. Mass Cytometry Reveals an Age-Related Increase in Prostate-Infiltrating Lymphocytes

(A) Workflow for mass cytometry (CyTOF) experiments in mouse. Prostates are removed, dissociated to single cells, stained with metal-tagged antibodies, and run on a mass cytometer.

(B) Frequencies of major immune cell populations in the prostates of adult and old B6 mice detected using CyTOF.

(C and D) t-SNE plots generated by clustering immune cells from adult and old mouse prostates based on expression of 14 surface markers detected with CyTOF.

(C) Heatmaps of t-SNE plot showing expression of eight selected markers, with scale on left. T cell and B cell regions are denoted by dotted line.
(D) t-SNE plots showing equal numbers of immune cells for adult (left), old (center), and both (right).
Data represent mean ± SEM of 5 biological replicates. **p < 0.01, ***p < 0.001.
See also Figure S2.

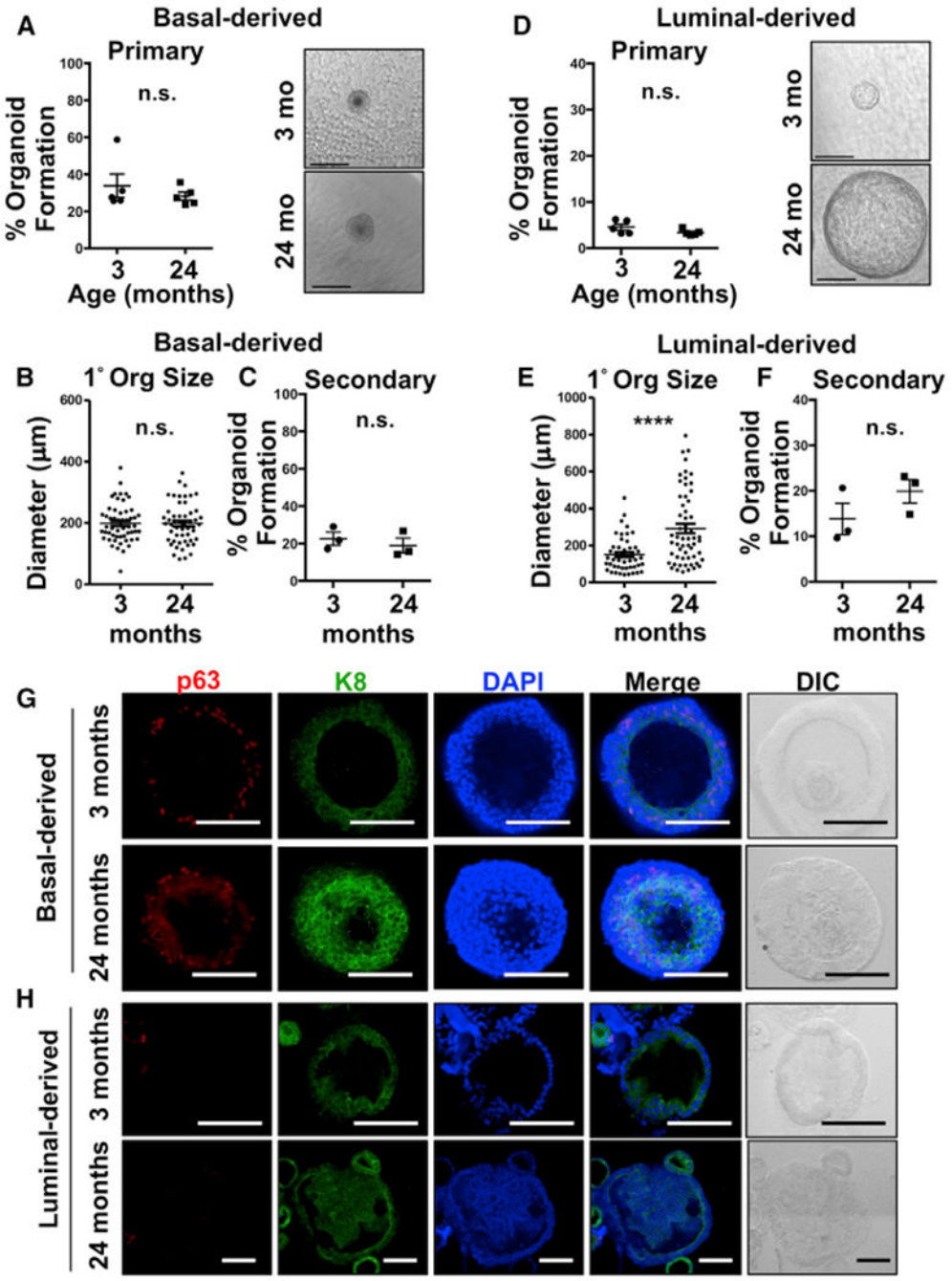

Figure 3. Epithelial Progenitor Activity Is Maintained in Old Mouse Prostate

(A) Primary organoid formation of sorted basal cells, shown as percentage of basal cells from 3- and 24-month-old mouse prostates that form organoids, with representative images shown on the right. Scale bars, 250 µm.

(B) Quantification of diameter of basal-derived primary organoids from 3- and 24-month-old mice.

(C) Percentage of single cells dissociated from primary basal-derived organoids that can generate secondary organoids.

(D) As in (A), with luminal cells from 3- and 24-month-old mouse prostates. Scale bars, 250 μm.

(E) As in (B), measuring organoids derived from luminal cells.

(F) As in (C), with organoids derived from luminal cells.

(G and H) Representative immunofluorescent and differential interference contrast (DIC) images of basal-derived (G) and luminal-derived (H) organoids from adult and old mice. Staining for p63 (red), K8 (Keratin 8, green), and DAPI (blue) individually and merged. Scale bars, 100 μm. Note: old luminal group is zoomed out to include large organoid. Data represent mean ± SEM of three to five biological replicates.

****$p < 0.0001$. n.s., not significant, $p \geq 0.05$. Mo, months of age.

See also Figure S3.

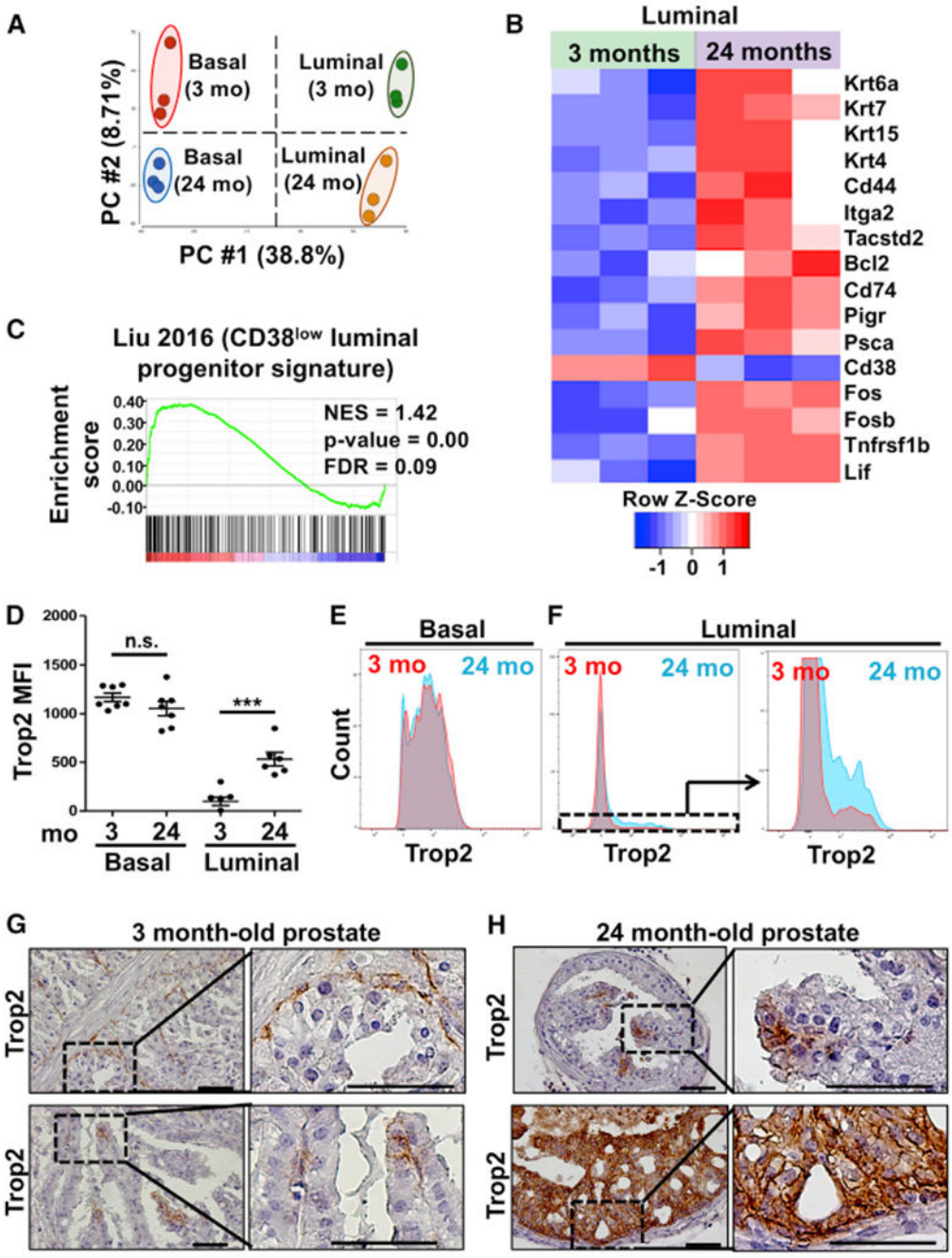

Figure 4. Increased Trop2 Expression in Luminal Cells from Old Mouse Prostate

(A) Principal component analysis of RNA sequencing data for basal and luminal cells from 3- and 24-month-old mice with three biological replicates per age.

(B) Heatmap of selected differentially expressed genes from RNA sequencing of luminal cells from 3- and 24-month-old mice with three biological replicates per age.

(C) Gene set enrichment analysis comparing 24-month-old mouse luminal cell signature with human CD38^{low} luminal cell signature, showing normalized enrichment score (NES) and false discovery rate (FDR).

(D) Trop2 mean fluorescence intensity (MFI) measured by flow cytometry in basal and luminal cells isolated from 3- and 24-month-old prostates with five to seven biological replicates per age. Data represent mean ± SEM.

(E and F) Histogram of Trop2 expression in basal cells (E) and luminal cells (F) from 3- and 24-month-old mice measured by flow cytometry.

(F) Boxed region on left is expanded in the right panel.

(G and H) Immunohistochemical analysis of representative prostate glands from adult (G) and old (H) mice stained for Trop2. Scale bars, 50 μm.

***$p < 0.001$. n.s. = not significant, $p \geq 0.05$. Mo = months of age.

See also Figures S4 and S5.

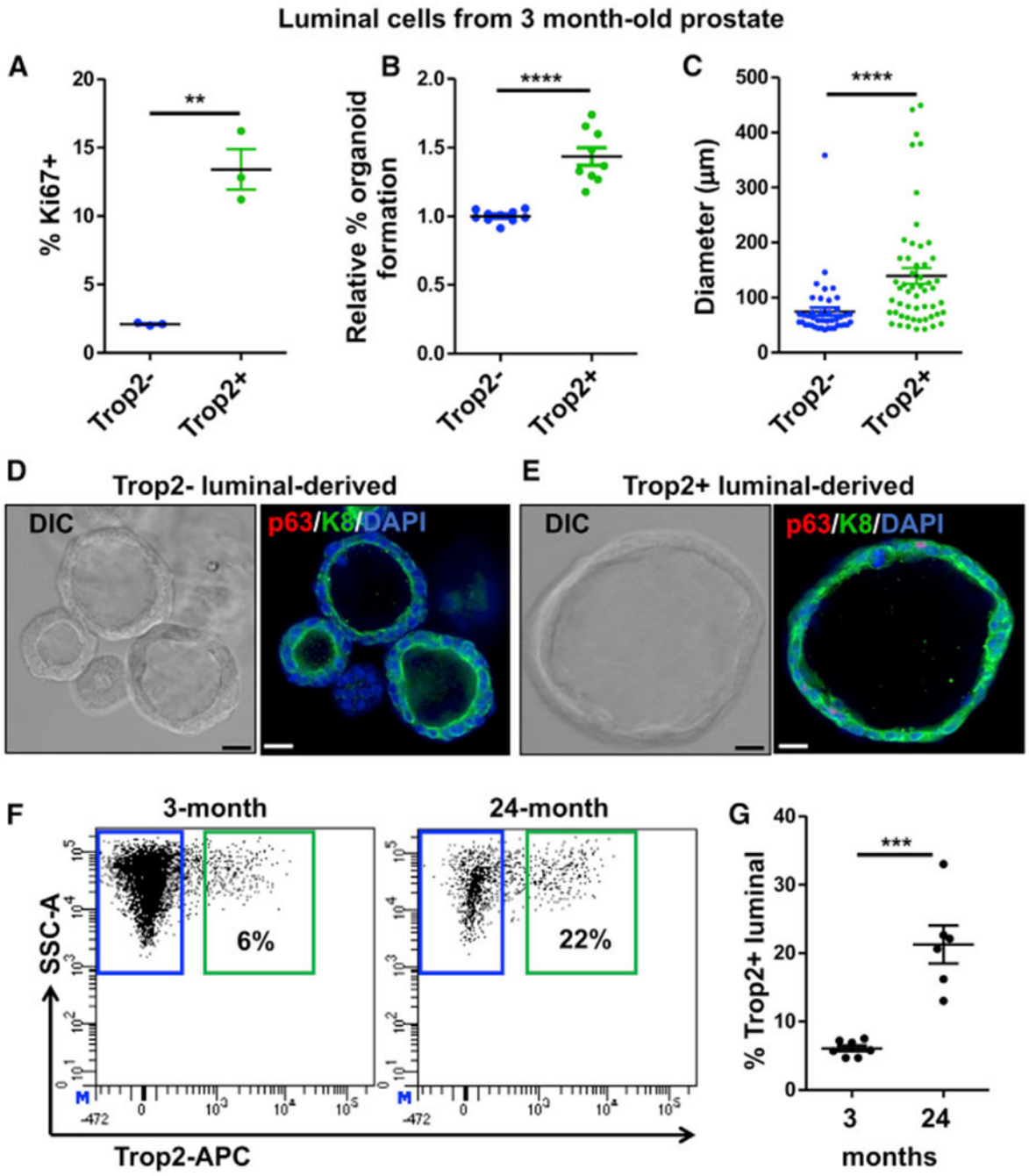

Figure 5. Trop2^{+} Luminal Cells Represent a Progenitor-Enriched Subpopulation that Is Expanded with Age

(A) Percentage of Ki67^{+} cells within the Trop2^{-} and Trop2^{+} luminal fractions from adult mice measured using intracellular flow cytometry with three biological replicates.

(B) Relative percent organoid formation of Trop2^{-} and Trop2^{+} luminal cells isolated from adult mouse prostate, normalized to Trop2^{-} luminal cells from each replicate experiment.

(C) Quantification of diameter of luminal-derived primary organoids from Trop2^{-} and Trop2^{+} luminal cells from adult mice.

(D and E) Representative differential interference contrast (DIC, left) and immunofluorescent images (right) of $Trop2^{-}$ luminal-derived (D) and $Trop2^{+}$ luminal-derived (E) organoids stained for p63 (red), K8 (green), and DAPI (blue). Three small organoids derived from $Trop2^{-}$ luminal cells are shown in (D). Scale bars, 20 μm.

(F) Representative flow cytometry plots illustrating the percentage of luminal cells that stain positively for Trop2 in adult and old mouse prostates. SSC-A, side scatter.

(G) The percentage of luminal cells that express Trop2 as measured by flow cytometry with six to seven biological replicates per age. Data represent mean ± SEM.

**$p < 0.01$, ***$p < 0.001$, ****$p < 0.0001$.

See also Figure S6.

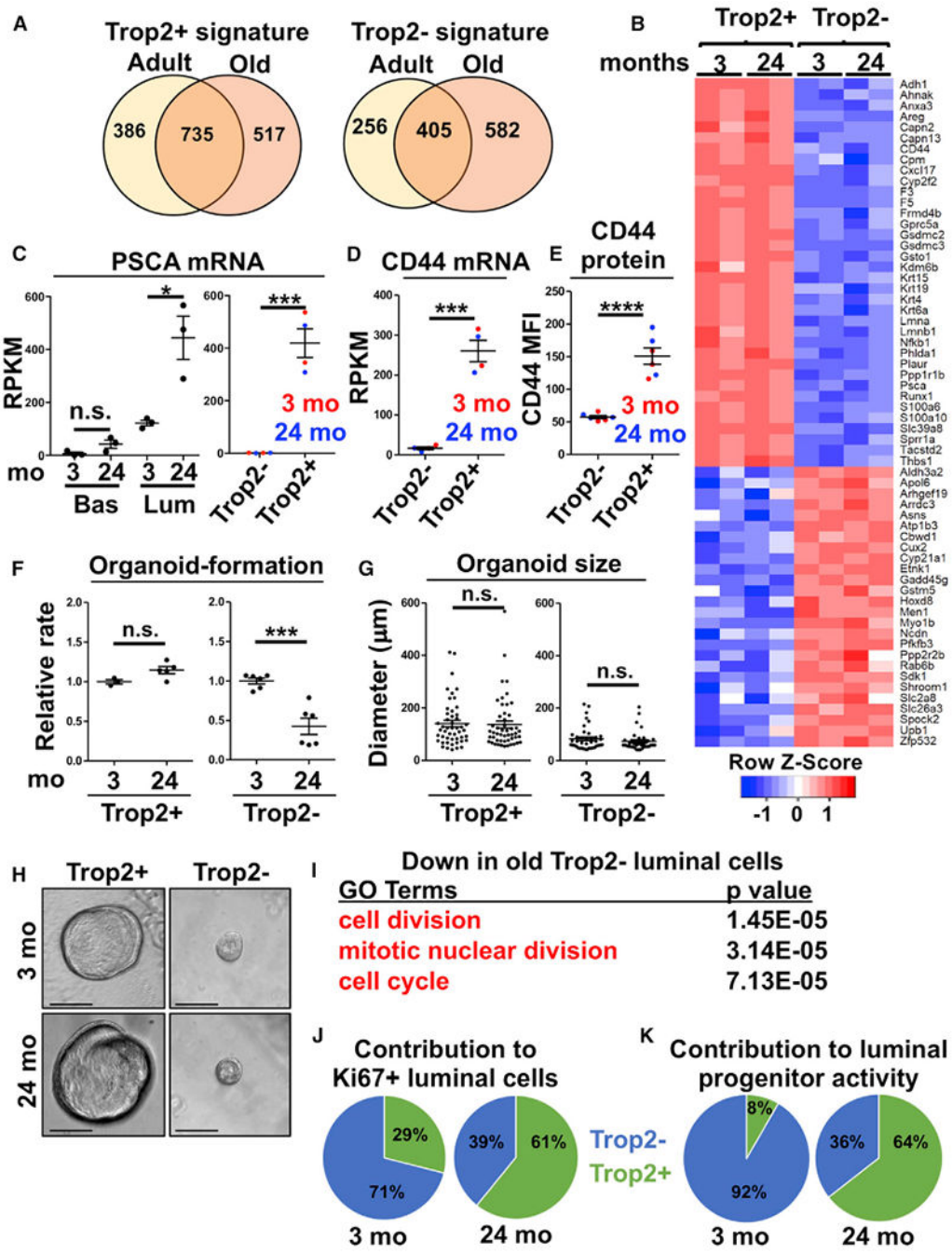

Figure 6. Trop2^{+} Luminal Signature and Progenitor Activity Are Maintained with Age

(A) Venn diagram shows the number of genes that are significantly upregulated in Trop2^{+} luminal cells (left) or Trop2^{-} luminal cells (right) from adult and old mouse prostate.

(B) Heatmap showing representative genes in the Trop2^{+} and Trop2^{-} luminal signatures, with biological replicates of each subset from adult and old mice.

(C) *Psca* mRNA in basal and luminal cells (left) and Trop2^{+} and Trop2^{-} luminal cells (right) shown as reads per kilobase of transcript per million mapped reads (RPKM).

(D) As in (C), with expression of *Cd44* in Trop2^{+} and Trop2^{-} luminal cells.

(E) Mean fluorescence intensity (MFI) of CD44 in $Trop2^+$ and $Trop2^-$ luminal cells from adult and old mice measured with flow cytometry.
(F) Relative percent organoid formation of $Trop2^-$ and $Trop2^+$ luminal cells isolated from adult and old prostate, normalized to adult prostate from each replicate experiment.
(G) Quantification of diameter of luminal-derived primary organoids from $Trop2^-$ and $Trop2^+$ luminal cells from adult and old mice. Data represent mean ± SEM.
(H) Representative images of organoids derived from adult and old $Trop2^+$ and $Trop2^-$ luminal cells. Scale bars, 100 μm.
(I) Gene ontology terms of gene sets downregulated in old compared with adult $Trop2^-$ luminal cells.
(J and K) Pie charts representing the contribution of $Trop2^-$ luminal (blue) and $Trop2^+$ luminal (green) cells to total proliferating ($Ki67^+$) luminal cells (J) and total luminal organoid formation (K). Relative rates of proliferation (J) or organoid formation (K) for $Trop2^+$ and $Trop2^-$ luminal cells were multiplied by the percentage of total luminal cells with a $Trop2^+$ or $Trop2^-$ phenotype, and represented as the ratio of total luminal proliferation or organoid formation from each subset.
*$p < 0.05$, ***$p < 0.001$, ****$p < 0.0001$. n.s. = not significant, $p \geq 0.05$. Mo = months of age.

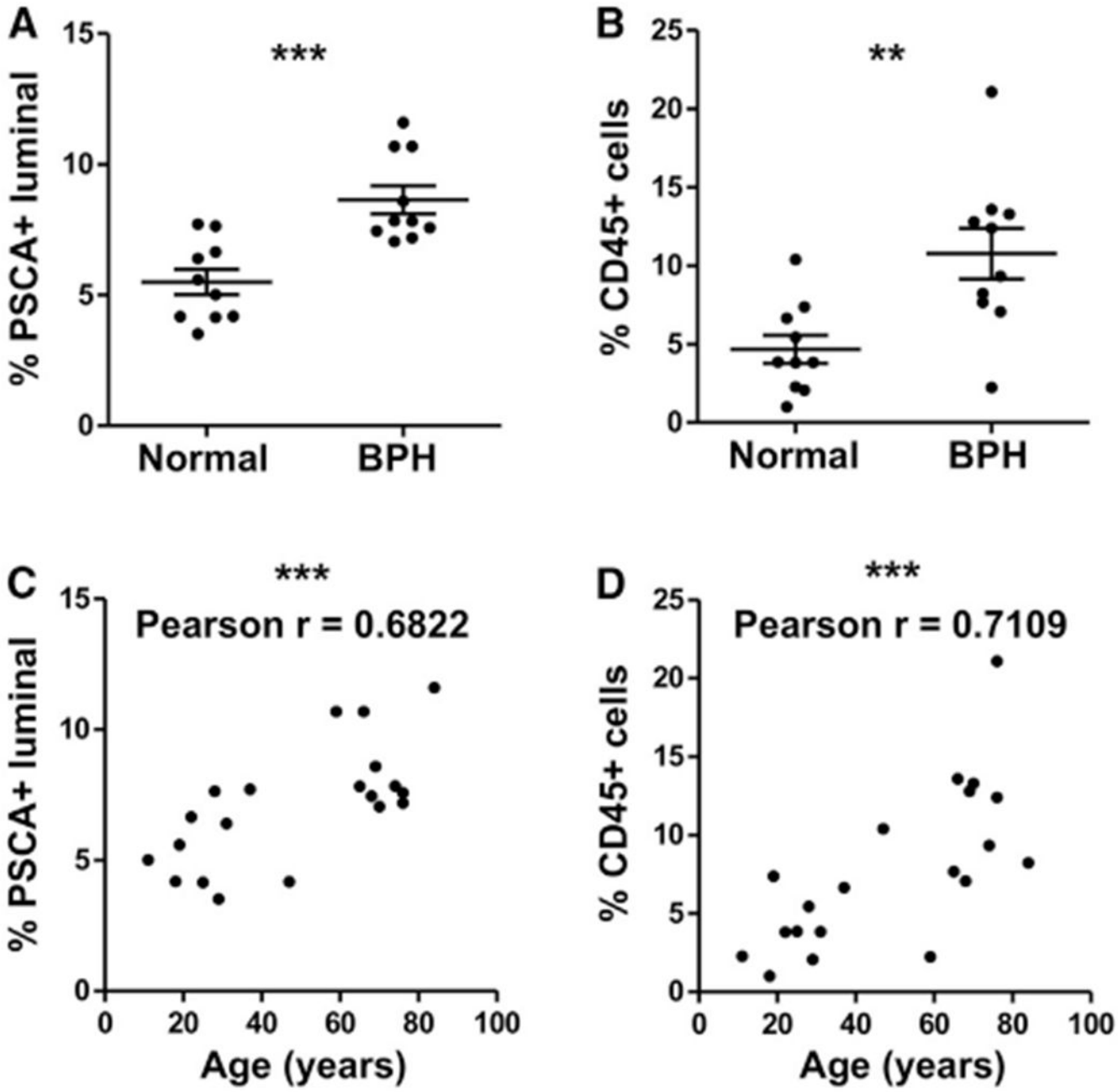

Figure 7. Human PSCA^{+} Luminal Cells and Inflammatory Cells Expand in Aging and BPH

(A) The percentage of luminal (CD45^{-} EpCAM^{+} PDPN^{-} CD26$^{low/+}$) cells that express PSCA in dissociated human prostate preparations from 10 men with BPH and 10 organ donors.

(B) As in (A), but measuring the percentage of total dissociated human prostate cells expressing CD45 as measured by flow cytometry. Data represent mean ± SEM.

(C) Plots showcorrelation between the percentage of luminal cells that express PSCA and patient age.

(D) Plots show correlation between the percentage of prostate cells that express CD45 and patient age.

**p < 0.01, ***p < 0.001.

KEY RESOURCES TABLE

REAGENT or RESOURCE	SOURCE	IDENTIFIER
Antibodies		
Rat anti-CD49f-PE	BioLegend	Cat#313612; RRID: AB_893373
Rat anti-EpCAM-APC/Cy7	BioLegend	Cat#118218; RRID: AB_2098648
Rat anti-CD31-FITC	BioLegend	Cat#102405; RRID: AB_312900
Rat anti-CD45-FITC	BioLegend	Cat#103107; RRID: AB_312972
Rat anti-Ter119-FITC	BioLegend	Cat#116205; RRID: AB_313706
Rat anti-ESAM-FITC	BioLegend	Cat#136205; RRID: AB_2044017
Goat anti-mouse TROP-2-APC	R & D Systems	Cat#FAB1122A; RRID: AB_2287133
Rat anti-CD44-FITC	BioLegend	Cat#103021; RRID: AB_493684
Rabbit anti-cytokeratin 5-Alexa Fluor 647	Abcam	Cat#ab193895; RRID: AB_2728796
Rabbit anti-cytokeratin 8-Alexa Fluor 488	Abcam	Cat#ab192467
Mouse anti-cytokeratin 14-FITC	Abcam	Cat#ab77684; RRID: AB_2265437
Mouse anti-cytokeratin 18-FITC	Abcam	Cat#ab52459; RRID: AB_869874
Rat anti-Ki67-FITC	BioLegend	Cat#652409; RRID: AB_2562140
Goat anti-mouse IgG-Alexa Fluor 488	Invitrogen	Cat#A28175; RRID: AB_2536161
Goat anti-rabbit IgG-Alexa Fluor 594	Invitrogen	Cat#A11012; RRID: AB_141359
Goat anti-rabbit IgG-Alexa Fluor 647	Invitrogen	Cat#A-21244; RRID: AB_141663
Goat anti-mouse IgG-Alexa Fluor 647	Invitrogen	Cat#A-21235; RRID: AB_141693
Goat anti-rabbit IgG, HRP-conjugated	Invitrogen	Cat#31463; RRID: AB_228333
Goat anti-mouse IgG, HRP-conjugated	Invitrogen	Cat#31430; RRID: AB_228307
Rabbit anti-goat IgG, HRP-conjugated	Invitrogen	Cat#31402; RRID: AB_228395
Rabbit anti-keratin 5	BioLegend	Cat#905504; RRID: AB_2616956
Goat anti-Tp63	R & D Systems	Cat#AF1916-SP; RRID: AB_2207174
Rabbit anti-p63	BioLegend	Cat#619002; RRID: AB_2207170
Goat anti-mouse TROP-2	R & D Systems	Cat# AF1122-SP; RRID: AB_2205662
Mouse anti-cytokeratin 8	BioLegend	Cat#904804; RRID: AB_2616821
Rabbit anti-Prom1	Abnova	Cat#PA312663; RRID: AB_10554766
Rabbit anti-Ki67	Abcam	Cat#ab15580; RRID: AB_443209
Mouse anti-tubulin	DSH3	Cat#12G10; RRID: AB_1157911
TruStain fcX (rat anti-mouse CD16/32) Antibody	BioLegend	Cat#101319; RRID: AB_1574973
Anti-mouse CD45 (clone 30-F11)-89Y	DVS	Cat#30890053; RRID: AB_2651152
Anti-mouse CD27 (clone LG.3A10)	BioLegend	Cat#124202; RRID: AB_1236456
Anti-mouse CD138 (clone 281-2)	BioLegend	Cat#142502; RRID: AB_10965646
Anti-mouse CD45R (clone RA3-6B2)-144Nd	DVS	Cat#31440113
Anti-mouse CD4 (clone RM4-5)-145Nd	DVS	Cat#31450023; RRID: AB_2687832
Anti-mouse F4/80 (clone BM8)-146Nd	DVS	Cat#31460083
Anti-mouse CD45 (clone 30-F11)-147Sm	DVS	Cat#31470033

REAGENT or RESOURCE	SOURCE	IDENTIFIER
Anti-mouse CD11b (clone M1/70)-148Nd	DVS	Cat#31480033
Anti-mouse CD3e (clone 145-2C11)-152Sm	DVS	Cat#31520043; RRID: AB_2687836
Anti-mouse CD25 (clone 3C7)	BioLegend	Cat#101913; RRID: AB_2562798
Anti-mouse Ly6C (clone HK1.4)-162Dy	DVS	Cat#31620143
Anti-mouse CD19 (clone 6D5)-166Er	DVS	Cat#31660153; RRID: AB_2687846
Anti-mouse CD8a (clone 53-6.7)-168Er	DVS	Cat#31680033
Anti-mouse CD117 (clone 2B8)	BioLegend	Cat#105802; RRID: AB_313211
Anti-mouse FcεR1a (clone MAR-1)-176Yb	DVS	Cat#3176006B
Anti-mouse CD11c (clone N418)-209Bi	DVS	Cat#3176006B
Anti-CD31 (clone WM59) BV421	BioLegend	Cat#303123; RRID: AB_2562179
Anti-CD26 (clone BA5b) APC	BioLegend	Cat#302709; RRID: AB_10913814
Anti-CD271 (clone ME20.4) PE	BioLegend	Cat#345105; RRID: AB_2282827
Anti-CD326 (clone EBA-1) BB515	BD	Cat#565398; RRID: AB_2728107
Anti-CD45 (clone HI30) PerCP/Cy5.5	Tonbo	Cat#65-0459; RRID: AB_2621897
Anti-CD200 (clone OX-104) BV711	BioLegend	Cat#329223; RRID: AB_2715824
Anti-PDPN (clone NC-08) PE	BioLegend	Cat#337004; RRID: AB_1595457
Rabbit anti-PSCA	Abcam	Cat#Ab64919; RRID: AB_1142338
Donkey anti-rabbit IgG BV421	DVS	Cat#406410; RRID: AB_10897810
Chemicals, Peptides, and Recombinant Proteins		
Collagenase type I	GIBCO	Cat#17-100-017
Deoxyribonuclease	Millipore Sigma	Cat#D4263-1VL
TrypLE express enzyme, no phenol red	GIBCO	Cat#12604-013
16% paraformaldehyde	Electron Microscopy Sciences	Cat#15710-S
Y-27632 dihydrochloride	Tocris Bioscience	Cat#1254
Saponin	Millipore Sigma	Cat#47036
Dispase	GIBCO	Cat#17105-041
Trypsin-EDTA	GIBCO	Cat#25300-054
Sodium azide	Millipore Sigma	Cat#S2271-100
Cell-ID intercalator-103Rh	Fluidigm	Cat#201103A
Cell-ID cisplatin	Fluidigm	Cat#201064
Cell-ID intercalator-Ir	Fluidigm	Cat#201192A
Maxpar® fix and perm buffer	Fluidigm	Cat#201067
Maxpar® cell staining buffer	Fluidigm	Cat#201068
EQ four element calibration beads	Fluidigm	Cat#201078
cOmplete protease inhibitor cocktail tablet	Roche	Cat#11697498001
Triton X-100	Thermo Fisher Scientific	Cat#BP151-100
A83-01	Tocris Bioscience	Cat#2939
Advanced DMEM/F-12	Thermo Fisher Scientific	Cat#12634010
B-27 Supplement (50x), Serum Free	Thermo Fisher Scientific	Cat#17504044

REAGENT or RESOURCE	SOURCE	IDENTIFIER
(DiHydro)testosterone (5α-Androstan-17β-ol-3-one)	Millipore Sigma	Cat#A-8380
GlutaMAX	Thermo Fisher Scientific	Cat#35050061
Matrigel GFR Membrane Matrix	Corning	Cat#CB-40230C
N-acetyl-L-cysteine	Millipore Sigma	Cat#A9165
Recombinant Human EGF, Animal-Free	PeproTech	Cat#AF-100-15
Recombinant Human Noggin	PeproTech	Cat#120-10C
Sucrose	Millipore Sigma	Cat#S0389-500G
4',6-diamidino-2-phenylindole (DAPI)	Thermo Fisher Scientific	Cat#D1306
Critical Commercial Assays		
Anti-Goat HRP-DAB Cell & Tissue Staining Kit	R & D Systems	Cat#CTS008; RRID: AB_10052005
Maxpar X8® multimetal labeling kit	Fluidigm	Cat#201300
RNeasy Mini Kit	QIAGEN	Cat#74104
KAPA stranded mRNA-seq kit	Roche	Cat#07962193001
Deposited Data		
Raw and processed RNaseq data (Adult and Old)	This paper	GEO: GSE122367
Raw and processed RNaseq data (Trop2^{+} and Trop2−)	This paper	GEO: GSE128724
Experimental Models: Organisms/Strains		
Mouse: C57BL/6J	Jackson Laboratories	Cat#000664
Mouse: C57BL/6N	UCLA Department of Radiation Oncology Animal Core Facility	N/A
Mouse: NSG	Jackson Laboratories and the UCLA Department of Radiation Oncology Animal Core Facility	Cat#005557
Software and Algorithms		
Sequencing Analysis Viewer (SAV)	Illumina	https://support.illumina.com/sequencing/sequencing_software/sequencing_analysis_viewer_sav.html
bcl2fastq Conversion Software V2.17	Illumina	https://support.illumina.com/sequencing/sequencing_software/bcl2fastq-conversion-software.html
Bowtie2 V2.1.0	Langmead and Salzberg, 2012	http://bowtie-bio.sourceforge.net/bowtie2/index.shtml
RNA-seq by Expectation-Maximization (RSEM) V1.2.15	Li and Dewey, 2011	http://deweylab.github.io/RSEM/
Empirical Analysis of Digital Gene Expression Data in R (edgeR)	Robinson et al., 2010	https://bioconductor.org/packages/release/bioc/html/edgeR.html
GOseq	Young et al., 2010	https://bioconductor.org/packages/release/bioc/html/goseq.html
Gene Set Enrichment Analysis (GSEA)	Subramanian et al., 2005	https://www.broadinstitute.org/gsea
Maxpar Panel Designer	Fluidigm	http://www.dvssciences.com/paneldesigner/resources
FlowJo V10	FlowJo LLC	https://www.flowjo.com/
Prism V7	GraphPad	https://www.graphpad.com/scientific-software/prism/
Other		

REAGENT or RESOURCE	SOURCE	IDENTIFIER
58Y1	Test Diet	Cat#1810473
35mm micro-dish	Ibidi USA	Cat#50-305-806
NuPAGE 4-12% Bis-Tris Gel	Novex	Cat#N P0335BOX
PVDF membrane	Millipore Sigma	Cat#IPVH00010
Sonic dismembrator	Thermo Fisher Scientific	Cat#FB120